




Charge multipole correlations and order in Cs_2TaCl_6 Aria Mansouri Tehrani ^{1,*}, Jian-Rui Soh,^{2,*} Jana Pásztorová ², Maximilian E. Merkel ¹, Ivica Živković,²
Henrik M. Rønnow,² and Nicola A. Spaldin^{1,†}¹Materials Theory, ETH Zurich, Wolfgang-Pauli-Strasse 27, 8093 Zürich, Switzerland²Institute of Physics, Ecole Polytechnique Federale de Lausanne (EPFL), CH-1015 Lausanne, Switzerland

(Received 26 July 2022; revised 29 September 2022; accepted 2 November 2022; published 26 January 2023)

We examine the role of charge, structural, and spin degrees of freedom in the previously poorly understood phase transition in the $5d^1$ transition-metal double perovskite Cs_2TaCl_6 using a combination of computational and experimental techniques. Our heat capacity measurements of single-crystalline Cs_2TaCl_6 reveal a clear anomaly at the transition temperature, T_Q , which was not previously observed in polycrystalline samples. Density functional calculations indicate the emergence of local charge quadrupoles in the cubic phase, mediated by the paramagnetic spins or local structural distortions which then develop into long-range-ordered charge quadrupoles in the tetragonal phase. Our resonant elastic x-ray scattering on Cs_2TaCl_6 single crystals lends support to our calculations. Our work provides insight into the phase transition in Cs_2TaCl_6 at T_Q , and demonstrates the utility of this unique combination of techniques in understanding the complex physics of hidden orders in paramagnetic spin-orbit-entangled compounds.

DOI: [10.1103/PhysRevResearch.5.L012010](https://doi.org/10.1103/PhysRevResearch.5.L012010)

In $3d^1$ transition-metal perovskites, the on-site Hubbard Coulomb repulsion, one-electron bandwidth, magnetic exchange, crystal-field splitting, and lattice strain energies are of similar size, and their competition results in a rich variety of ground states, ranging from correlated metals (SrVO_3 and CaVO_3) [1] to antiferromagnetic (LaTiO_3) [2] and ferromagnetic (YTiO_3) [3] insulators. The crystal structures exhibit symmetry-lowering phase transitions to states with tilts and rotations of the oxygen octahedra, as well as Jahn-Teller distortions related to the lifting of orbital degeneracy.

In $5d^1$ double perovskites, in which half of the B -site cations are either absent or replaced by nonmagnetic ions, the B -site dilution reduces the bandwidth so that it is again comparable in energy to the other interactions listed above [4]; enhanced spin-orbit coupling from the heavy B -site cations and magnetic frustration associated with their face-centered-cubic arrangement further increase the manifold of competing interactions. The phase diagram resulting from a model Hamiltonian containing these interactions [5] includes ferromagnetic and antiferromagnetic phases with magnetic octupolar order dominating over the usual dipolar order, and charge quadrupole-ordered paramagnetism, as well as a possible quantum-spin-liquid state.

Experimental studies of $5d^1$ double perovskites have focused on the oxides such as $\text{Ba}_2\text{NaOsO}_6$ and $\text{Ba}_2\text{MgReO}_6$,

both of which show two phase transitions in measurements of their specific heat as a function of temperature. The low-temperature phase transition, T_M , occurring at ~ 7 K and ~ 18 K, respectively, corresponds to the formation of the magnetically ordered state, which in both cases is a strongly canted antiferromagnet with a net magnetization [6–9]. The higher-temperature transition (at $T_Q \sim 10$ K for $\text{Ba}_2\text{NaOsO}_6$ and ~ 33 K for $\text{Ba}_2\text{MgReO}_6$) has been attributed to the ordering of charge quadrupoles on the d^1 B -site cations and is accompanied by a small structural distortion, detectable only with high-resolution x-ray diffraction [6–10]. Recently, the chlorides $A_2\text{TaCl}_6$ ($A = \text{K}, \text{Rb}, \text{Cs}$) have also attracted some attention, motivated by their greater ionicity, which positions them closer to the formal d^1 limit [11,12]. In this work, we focus our attention on Cs_2TaCl_6 .

Cs_2TaCl_6 is a vacancy-ordered double perovskite which crystallizes in the cubic $Fm\bar{3}m$ space group at room temperature with lattice constant $a = 10.3285(4)$ Å based on experimental powder x-ray diffraction data [11]. Heat capacity measurements indicate an almost complete recovery of the electronic entropy of $R \ln 4$, which corresponds to the ideal $J_{eff} = 3/2$ quartet state as expected for a $5d^1$ Ta ion in an ideal octahedral environment. Upon cooling, the $R \ln 4$ can be accounted for by assuming, first, the ordering of the multipolar (magnetic or charge) degree of freedom, followed by the ordering of magnetic dipoles. While the latter is seen from the pronounced peak in the heat capacity measurements at $T_M \sim 4$ K, no clear signature of the former has been seen in earlier studies on the powder sample of Cs_2TaCl_6 . Instead, it has been proposed that in addition to the ordering of magnetic dipoles, fluctuating short-ranged orders of entangled multipoles such as charge quadrupoles are responsible for the full recovery of $R \ln 4$ [11]. Furthermore, it has been shown that Cs_2TaCl_6 undergoes a structural phase transition to tetragonal symmetry

*These authors contributed equally to this work.

†nicola.spaldin@mat.ethz.ch

($a = 7.29 \text{ \AA}$, and $c = 10.16$ lattice parameters) with $I4/mmm$ space group around 30 K; this symmetry allows a ferroic ordering of the charge quadrupoles on the Ta sites [11].

In the current Letter, we combine state-of-the-art computational and experimental techniques to study the previously poorly understood phase transition reported in Cs_2TaCl_6 at T_Q . Specifically, we revisit the specific heat measurements, where surprisingly no anomaly was previously observed [11], and explore the nature of the proposed multipolar fluctuations around the phase transition [11]. To achieve these objectives, we synthesize polycrystalline and single-crystalline Cs_2TaCl_6 and perform a comparative study of their heat capacities. Second, we use single-crystal x-ray diffraction to detect structural changes at T_Q . In addition, we use density functional theory (DFT) and resonant x-ray diffraction to look for evidence of local multipoles and their entanglements to the structural phase transition in the vicinity of T_Q . Finally, we discuss the possible role of higher-order charge multipoles at the transition at T_Q .

The Cs_2TaCl_6 single crystals were synthesized following the procedure for K_2TaCl_6 in Ref. [11]. CsCl and TaCl_5 powders were mixed in a ratio of 2:1 and placed in a quartz tube with Ta metal wire. The tube was evacuated using a mechanical and turbo pump, then sealed and heated to $600 \text{ }^\circ\text{C}$, where it was held for 36 hours. The system was then cooled down to $500 \text{ }^\circ\text{C}$ with a slow cooling rate of $0.5 \text{ }^\circ\text{C/h}$. Since the starting materials and final product are air-sensitive, all processes were performed in the glove box with Ar atmosphere. Dark purple single-crystal plaquettes were obtained and could be cleaved easily along the (111) plane. The quality of the single crystals was checked using a Rigaku Synergy-I XtaLAB x-ray diffractometer. Heat capacity measurements on the Cs_2TaCl_6 single crystals were also performed on a physical property measurement system (PPMS) down to $T = 2 \text{ K}$, as shown in Fig. 1(a).

Polycrystalline Cs_2TaCl_6 was synthesized by the solid-state reaction method described in Ref. [11]. To identify structural changes in Cs_2TaCl_6 , synchrotron x-ray diffraction was performed on polycrystalline Cs_2TaCl_6 at the MS-powder beamline at the Swiss Light Source (PSI). The powder was filled in borosilicate glass capillaries with a diameter of 0.3 mm , which were then closed with grease and sealed before the experiment. Measurements were performed with an incident x-ray wavelength of 0.563 \AA and to temperatures down to 4.2 K [see Fig. 2(a)]. The heat capacity measurements of polycrystalline Cs_2TaCl_6 were performed on a PPMS (Quantum Design) down to $T = 2 \text{ K}$, as shown in Fig. 2(b).

We first present our heat capacity measurements and analyze them for indications of phase transitions, particularly of multipolar order. Figure 1(a) shows the heat capacity of our single-crystalline Cs_2TaCl_6 as a function of temperature. An anomaly at $T_M = 4.6 \text{ K}$ is observed in the heat capacity curve, which is concomitant with the onset of the magnetic dipolar order of Ta ions and is consistent with an earlier report [11] and our measurements of the heat capacity of polycrystalline Cs_2TaCl_6 as shown in Fig. 2(a). Furthermore, the temperature dependence of the heat capacity of single-crystalline Cs_2TaCl_6 also displays a kink at $T_Q \sim 15 \text{ K}$, which was not observed in our polycrystalline samples or reported in the polycrystalline samples of Ref. [11]. The observation of a

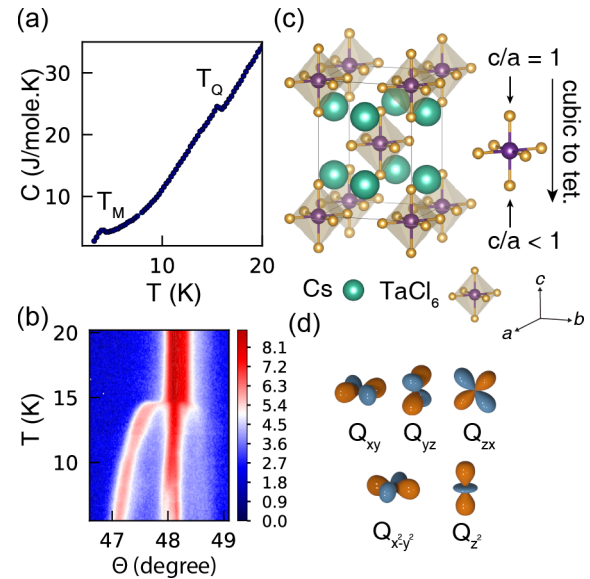


FIG. 1. (a) Measured heat capacity of single-crystalline Cs_2TaCl_6 as a function of temperature. The heat capacity curves display an anomaly at T_M , and an additional one at T_Q . (b) Synchrotron x-ray diffraction pattern of Cs_2TaCl_6 as a function of T shows a splitting of the $(777)_c$ peak below T_Q . (c) Crystal structure of Cs_2TaCl_6 in the reduced unit cell representation. (d) Sketch of the charge quadrupoles in Cartesian representation. The orange and cyan regions represent regions with excess and reduced electronic charge.

peak in the heat capacity at T_Q in single-crystalline Cs_2TaCl_6 clearly indicates a phase transition at this temperature. This resolves the earlier apparent “mystery” regarding the absence of an anomaly in the heat capacity in polycrystalline Cs_2TaCl_6 which was attributed to the buildup of a hidden order [11]. One possible reason why polycrystalline Cs_2TaCl_6 (in both Ref. [11] and our work) does not manifest an anomaly at

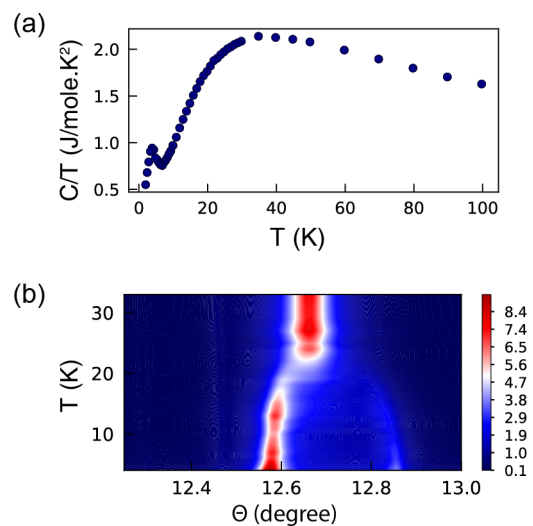


FIG. 2. (a) Temperature dependence of the $(4, 0, 0)_c$ reflection of polycrystalline Cs_2TaCl_6 , which splits into the $(2, 2, 0)_t$ and $(0, 0, 4)_t$ reflections below $T_Q \sim 28 \text{ K}$. (b) The temperature dependence of the heat capacity of polycrystalline Cs_2TaCl_6 displays only one anomaly at $T \sim 4 \text{ K}$.

T_Q could be due to sample inhomogeneity of the polycrystalline Cs_2TaCl_6 or the small size of the polycrystalline grains, broadening the transition.

Having unambiguously established the presence of a phase transition at T_Q , we next study the relative roles of charge quadrupoles, magnetic dipoles, and lattice distortions in driving the transition, considering the temperature regimes $T < T_Q$ and $T > T_Q$ in turn.

Now we study the evolution of the crystal structure of single-crystalline Cs_2TaCl_6 as a function of temperature, using x-ray diffraction. The single-crystalline diffraction pattern of Cs_2TaCl_6 at $T = 300$ K is fully consistent with the $Fm\bar{3}m$ (No. 225) space group, in good agreement with earlier reports [11,12]. The refinement of our temperature-dependent polycrystalline x-ray diffraction patterns [see Fig. 2(b)] indicates that Cs_2TaCl_6 undergoes a symmetry lowering below $T \sim 28$ K, to the tetragonal $I4/mmm$ (No. 139) space group, consistent with Ref. [11] where an accompanying anomaly in the heat capacity measurements was also absent [see Fig. 2(a)]. Structurally, this symmetry lowering manifests as a compression of the TaCl_6 octahedron along z with a reduction of the lattice parameter c_t such that $c_t < \sqrt{2}a_t$.

In Fig. 1(b) we show the temperature dependence of the single-crystal x-ray diffraction of Cs_2TaCl_6 . The $(777)_c$ reflection shown in Fig. 1(b) splits below 15 K into the $(707)_t$ peaks, concomitant with the observed anomaly in single-crystal heat capacity measurements. We, therefore, assign this structural transition to T_Q . Note that this occurs at a significantly lower temperature compared to the polycrystalline Cs_2TaCl_6 reported in this work and in Ref. [11]. The $(777)_c \rightarrow (707)_t$ peak splitting at T_Q , is consistent with the cubic-to-tetragonal distortion seen in polycrystalline Cs_2TaCl_6 , as shown in Fig. 1(c), and is due to the threefold freedom in the choice of the compression axis (z) in the tetragonal distortion of a cubic structure (along either a , b , or c), which gives rise to three structural domains and hence the split peaks. Since the multiplicity of peaks in single-crystal diffraction is always 1, the reason for the peak splitting of $(707)_t$ below T_Q is subtly different from the reason for the peak splitting observed in the polycrystalline diffraction pattern of Cs_2TaCl_6 , which is due to the multiplicity. Nonetheless, the physical origin of the peak splitting is the same, driven by the compression of the TaCl_6 octahedron.

While the crystal structural distortion at T_Q as well as the anomaly in the heat capacity are indicative of the long-ranged ordering of charge quadrupoles, as pointed out previously [11], they are not thoroughly studied yet. As a first step in this direction, we use first-principles calculations based on DFT to search for the various charge quadrupole components [Fig. 1(b)] and determine how they interact with the crystal structure. For Cs_2TaCl_6 , the B -site cations (Ta) occupy centrosymmetric lattice sites, and so only even-ranked charge multipoles, charge quadrupoles, and hexadecapoles, and odd-ranked magnetic multipoles, magnetic dipoles, and octupoles can be nonzero [13]. In this work, we first focus on determining the existence and ordering of the charge quadrupoles and later discuss the possible role of the charge hexadecapoles in the phase transition at T_Q .

Since standard density functional calculations with periodic boundary conditions yield the zero-kelvin magnetically

ordered state, they are not immediately appropriate for describing the regime of interest here, in which the local magnetic dipoles on the Ta sites are not ordered. In this work, we adopt a method similar to that introduced in Ref. [14] and Ref. [15], which we recently applied to $\text{Ba}_2\text{MgReO}_6$ [16], and construct a supercell containing randomly oriented magnetic dipoles, constrained to have zero total magnetization, as shown in Fig. 3(c).

All DFT calculations were performed using the Vienna *ab initio* simulation package (VASP) using a plane-wave basis set. Projector augmented wave pseudopotentials [17–20] Cs_{sv}, Ta, and Cl as provided by VASP were used in conjunction with the Perdew-Burke-Ernzerhof (PBE) functional [21] and on-site effective Hubbard $U_{eff} = 2\text{eV}$ correction for the Ta $5d$ orbitals [22]. Spin-orbit coupling was included explicitly. An energy cutoff of 600 eV and gamma-centered k -point meshes of $8 \times 8 \times 6$ and $2 \times 2 \times 1$ were used for the tetragonal unit cell and the supercells, respectively.

The multipole moments were calculated by decomposing the DFT charge [23] or spin [24] densities in the spheres around the atomic sites into their component charge or magnetic multipoles. In this implementation, the local multipole moments are obtained by decomposing the DFT density matrix into the components of the irreducible spherical tensor centered on the ions. For details of the formalism, see Ref. [23]. The local on-site exchange energy, E_x , is reformulated in terms of the multipolar decomposition of the density matrix following Ref. [25]. This method has already been implemented in the all-electron full-potential linearized augmented plane wave ELK code [26]. Here, we have implemented this method within an open-source Python code Multipyles (see Ref. [27]) compatible with any electronic structure calculation code.

Figure 3(b) shows the calculated charge quadrupole components on the 16 Ta sites of our Cs_2TaCl_6 supercell constructed in the low-temperature experimental $I4/mmm$ crystal structure with the magnetic dipole moments constrained to random orientations with a net-zero total magnetization. The only nonzero charge quadrupoles in the paramagnetic state are the Q_{z^2} ; these all have the same sign and are close to the same magnitude, indicating ferroic ordering. The ferroic ordering of the Q_{z^2} quadrupoles is consistent with the crystal structure distortion that results in the contraction of Ta-Cl bonds along the z axis by ≈ 0.4 Å. The absence of any antiferroic ordering is consistent with the absence of other types of distortion, as also revealed by x-ray diffraction data.

Having discussed the long-ranged order of the lattice distortion and charge quadrupoles in the paramagnetic phase below T_Q , we now turn to the magnetic dipole, crystal structure, and charge degrees of freedom above T_Q . In particular, we investigate the proposal of Ref. [11] that short-ranged order in charge quadrupoles persists even when Cs_2TaCl_6 is in its high-symmetry cubic crystal structure.

We use resonant elastic x-ray scattering to look for evidence of short-ranged ferroic order of Q_{z^2} charge quadrupoles above the structural transition. Performing resonant elastic x-ray scattering (REXS) at the Ta L_3 edge has the threefold benefit of (1) direct coupling to the Ta ions, (2) strong resonant enhancement of the scattered signal, and (3) sensitivity to any

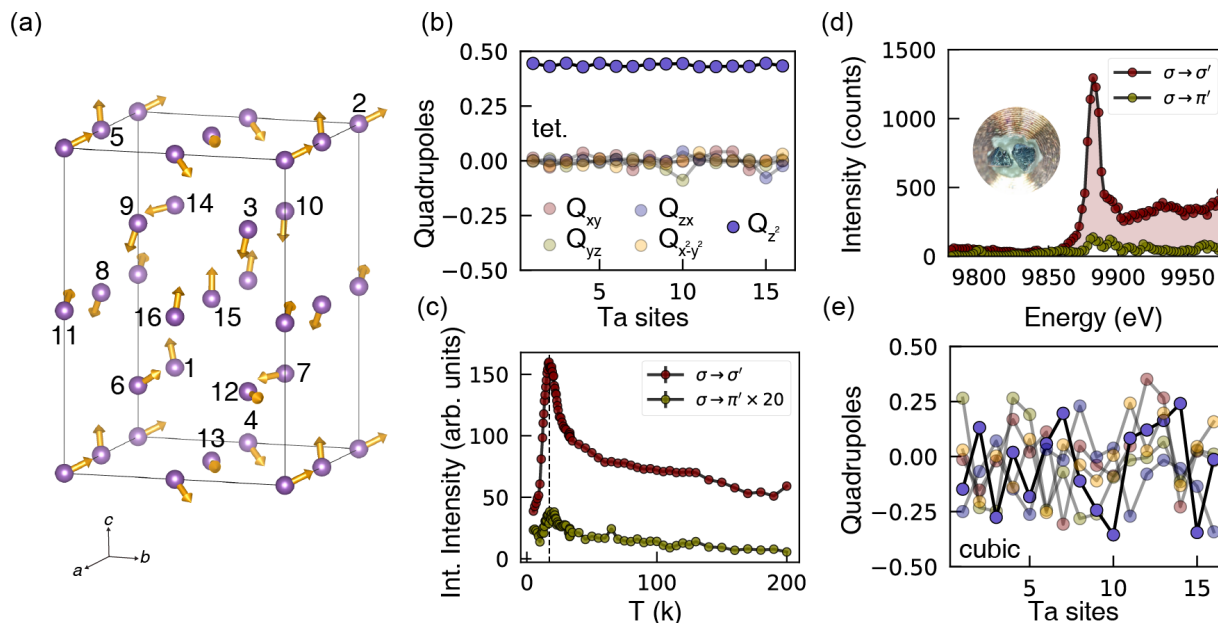


FIG. 3. (a) Paramagnetic supercell of Cs_2TaCl_6 used for DFT calculations. Only Ta atoms are shown for clarity. (b) Calculated charge quadrupoles on the Ta atoms labeled as in panel (a) in units of electron charges in the tetragonal crystal structure. (c) Temperature dependence of the integrated intensity of the $(777)_c$ and $(707)_t$ reflections above and below T_Q (dashed line) measured with REXS. (d) The summed intensity of the $(777)_c$ reflection of Cs_2TaCl_6 as a function of incident x-ray energy measured at $T = 20$ K in the $\sigma \rightarrow \sigma'$ and $\sigma \rightarrow \pi'$ scattering channels. The inset shows the cleaved (111) faces of the flux-grown Cs_2TaCl_6 crystals. (e) The magnitude of charge quadrupole components on the 16 Ta sites of the supercell of Cs_2TaCl_6 in units of electron charges in the cubic setting.

asphericity of the $5d^1$ electron cloud density which yields directly the charge quadrupoles.

The REXS measurement was performed on a single-crystalline Cs_2TaCl_6 on the 6-circle diffractometer in the EH1 hutch of the P09 hard x-ray beamline at the PETRA III storage ring (DESY). The incident x-ray energy was tuned to close to the Ta L_3 absorption edge ($E \sim 9881$ eV), and the polarization of the scattered beam (in vertical scattering geometry) was analyzed with a Cu(400) analyzer to differentiate between the $\sigma \rightarrow \sigma'$ and $\sigma \rightarrow \pi'$ scattering events. As Cs_2TaCl_6 is moderately air-sensitive, the single crystal was freshly cleaved just prior to the REXS measurement.

In the $Fm\bar{3}m$ space group, our structure factor calculation indicates that the coherently scattered x-rays arising from the ferroic Q_{z^2} charge quadrupole order coincide with the structural peaks in reciprocal space. Differentiating between the different contributions to the intensity of the scattered x-rays is difficult since both scattering processes benefit from resonant enhancement. To minimize the structural contributions to the scattered intensity, we chose a reflection with a small structure factor, namely the $(777)_c$ peak. Figure 3(c) shows the temperature dependence of the integrated intensity of the peak in the $\sigma \rightarrow \sigma'$ and $\sigma \rightarrow \pi'$ scattering channels. Notably, at all temperatures above T_M , we observe that the intensity is mainly in the $\sigma \rightarrow \sigma'$ channel, implying that the observed peak intensity is dominated by scattering processes that preserve the photon polarization. Such behavior arises from charge quadrupoles and the crystal structure but not from magnetic dipoles.

Our main result is an anomalous increase in the intensity of the $(777)_c$ reflection in the $\sigma \rightarrow \sigma'$ scattering channel

on cooling toward T_Q . Given that the structure of Cs_2TaCl_6 does not change above T_Q , this additional scattering intensity cannot be explained by conventional Bragg scattering. In addition, we see a strong peak at the Ta L_3 edge in the energy dependence of the scattered x-rays at $T = 20$ K [Fig. 3(d)], indicating that the scattering is coming mainly from the Ta ions. We conclude that it arises from disordered local charge quadrupoles, which also give rise to scattering processes that preserve the x-ray polarization. The sharp drop in the peak intensity below T_Q arises from the splitting of the $(707)_t$ peak below T_Q , as described in the earlier section.

To assist in interpreting the origin of the extra intensity of the $\mathbf{Q} = (777)_c$ reflection above T_Q , we now perform DFT calculations with Cs_2TaCl_6 constrained to its cubic crystal structure. We construct a supercell with disordered Ta local moments, as in Fig. 3(b), but using the high-temperature $Fm\bar{3}m$ experimental structure. Figure 3(e) shows the calculated components of the charge quadrupoles on the Ta sites for this case. Note that while all the charge quadrupoles are inconsistent with the cubic crystal structure symmetry, they are nonzero because the spin lowers the local symmetry. We find that the variation of the charge quadrupoles in the cubic crystal structure is large, of the order of around 0.5 electron charges. Such large variations indicate that all charge quadrupole components can be finite and significant following the spin direction in the cubic environment due to the spin-orbit-entangled nature of the $5d^1$ electron in Cs_2TaCl_6 . Our analysis confirms that charge quadrupoles exist even in the cubic setting at $T > T_Q$, consistent with our interpretation of the REXS data [Fig. 3(c)]. In our DFT model, these variations are the consequence of the spin moment fluctuations; however

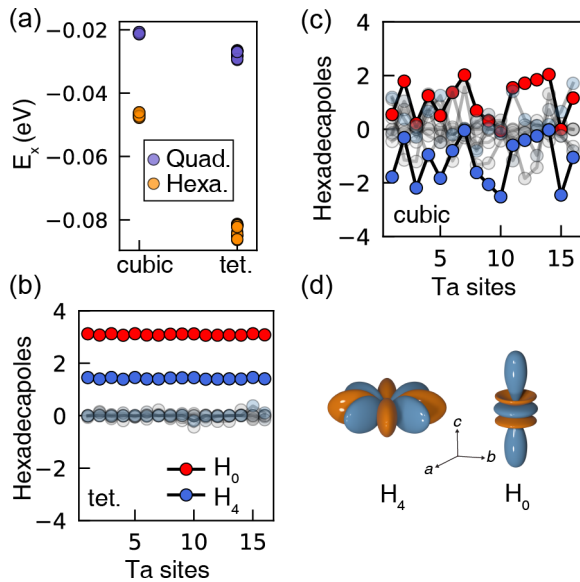


FIG. 4. (a) Exchange energies of the charge quadrupoles and hexadecapoles calculated for cubic and tetragonal phases of Cs_2TaCl_6 . (b) The calculated charge hexadecapoles in the tetragonal phase of Cs_2TaCl_6 for the atoms labeled in Fig. 2(a). (c) The calculated charge hexadecapoles in the cubic phase of Cs_2TaCl_6 for the Ta atoms labeled in Fig. 2(a). (d) The shapes of charge hexadecapole components, the H_0 and H_4 .

they would also be induced by local crystal structure distortions.

Finally, we follow the approach of Ref. [25], and calculate the contribution of the quadrupoles as well as the symmetry-allowed next-order charge multipoles, the hexadecapoles, to the total on-site exchange energy (E_x) for both cubic and tetragonal phases. Reference [25] demonstrated that the multipole channel corresponding to the most negative E_x has the main energetic contribution to the phase transition and can be considered as a primary order parameter. Figure 4(a) shows the calculated E_x 's on all 16 Ta ions (in the supercells) in both the cubic and tetragonal settings. Interestingly, in both crystal structures, charge hexadecapoles comprise the main contribution to the E_x (the magnetic multipoles are not shown here as they do not order). Furthermore, we observe that the E_x values for both charge quadrupoles and hexadecapoles are more negative for the tetragonal phase, indicating that the structural phase transition at T_Q stabilizes them further.

Here, we use a simplified notation for charge hexadecapoles (rank 4 tensor), H_t , where $-4 \leq t \leq 4$ as described in the Ref. [25] formalism. In Figs. 4(b) and 4(c) we plot the charge hexadecapole components for the 16 Ta sites of the supercell for both the tetragonal and cubic symmetries of Cs_2TaCl_6 . When the symmetry of the supercell is constrained to the tetragonal symmetry (corresponding to $T < T_Q$), two nonzero components of the charge hexadecapoles, H_0 and H_4 [illustrated in Fig. 4(d)], order ferroically while all other

components are calculated to be close to zero. Unlike the charge quadrupoles, however, the H_0 and H_4 components of the charge hexadecapoles tend to order ferroically in the cubic setting (corresponding to $T > T_Q$) as shown in Fig. 4(c). Therefore, despite the large negative E_x , the charge hexadecapoles cannot be viewed as the primary order parameter associated with the transition.

We provided an in-depth description of the origin of phase transitions in spin-orbit-entangled $5d$ transition-metal double perovskites by analyzing the coupled spin, charge, multipole, and structural order in Cs_2TaCl_6 . First, we synthesized a single crystal of Cs_2TaCl_6 and detected a new anomaly in the heat capacity measurements at temperature T_Q previously associated with a poorly understood phase transition. Then, we used single-crystal x-ray diffraction to determine the cubic-tetragonal structural changes at this temperature. Our DFT calculations confirmed that charge quadrupoles order ferroically for the tetragonal low-temperature phase, consistent with our measured compression of Ta-Cl bonds along z . Furthermore, our DFT methodology enables the study and understanding of the complex interaction of higher-order charge, crystal structure, and local spin moments in transition-metal compounds. In the region $T > T_Q$ our temperature-dependent REXS measurements showed a steady buildup of short-ranged order on approaching T_Q . Our DFT calculations further corroborated the REXS observations suggesting that this could result from disordered local charge quadrupole moments in the cubic high-temperature phase driven either by local structural distortions or the paramagnetic nature of the spin moments at $T > T_M$, or a combination of both.

In further work, a decisive proof of multipolar order with REXS will require a material in which the structural peaks do not coincide with the resonant charge quadrupolar or magnetic dipolar peaks. In double perovskite $5d^1$ systems, this could be achieved if charge/magnetic multipoles order antiferroically. In addition, a large magnitude of multipole moments is desirable for successfully detecting hidden orders. Hence, an essential task in the subsequent investigations of hidden order in $5d^1$ double perovskites that are amenable to the existing techniques is identifying new materials possessing large multipole moments with antiferroic long-ranged order.

This work was funded by the European Research Council (ERC) under the European Union's Horizon 2020 research and innovation program projects HERO (Grant No. 810451) and CALIPSOPlus (Grant No. 730872). The beamline proposal numbers for the Cs_2TaCl_6 experiments are I-20210904 EC (P09, DESY) and 20210818 (MS-POWDER, SLS). We thank S. Francoual and A. Cervellino for assistance during the various experiments. Calculations were performed at the Swiss National Supercomputing Centre (SCS) under Project IDs s889 and eth3 and on the EULER cluster of ETH Zürich. J.-R.S. acknowledges support from the Singapore National Science Scholarship from the Agency for Science Technology and Research.

- [1] K. Morikawa, T. Mizokawa, K. Kobayashi, A. Fujimori, H. Eisaki, S. Uchida, F. Iga, and Y. Nishihara, Spectral weight transfer and mass renormalization in Mott-Hubbard systems SrVO_3 and CaVO_3 : Influence of long-range Coulomb interaction, *Phys. Rev. B* **52**, 13711 (1995).
- [2] C. C. Hays, J.-S. Zhou, J. T. Markert, and J. B. Goodenough, Electronic transition in $\text{La}_{1-x}\text{Sr}_x\text{TiO}_3$, *Phys. Rev. B* **60**, 10367 (1999).
- [3] H. D. Zhou and J. B. Goodenough, Evidence for two electronic phases in $\text{Y}_{1-x}\text{La}_x\text{TiO}_3$ from thermoelectric and magnetic susceptibility measurements, *Phys. Rev. B* **71**, 184431 (2005).
- [4] K. Samanta and T. Saha-Dasgupta, Comparative study of electronic structure and magnetic properties of osmate double perovskites: $\text{Ca}_2\text{FeOsO}_6$ versus $\text{Ca}_2\text{Co(Ni)OsO}_6$, *J. Phys. Soc. Jpn.* **87**, 041007 (2018).
- [5] G. Chen, R. Pereira, and L. Balents, Exotic phases induced by strong spin-orbit coupling in ordered double perovskites, *Phys. Rev. B* **82**, 174440 (2010).
- [6] W. Liu, R. Cong, E. Garcia, A. P. Reyes, H. O. Lee, I. R. Fisher, and V. F. Mitrović, Phase diagram of $\text{Ba}_2\text{NaOsO}_6$, a Mott insulator with strong spin orbit interactions, *Phys. B: Condens. Matter* **536**, 863 (2018).
- [7] L. Lu, M. Song, W. Liu, A. P. Reyes, P. Kuhns, H. O. Lee, I. R. Fisher, and V. F. Mitrović, Magnetism and local symmetry breaking in a Mott insulator with strong spin orbit interactions, *Nat. Commun.* **8**, 14407 (2017).
- [8] D. Hirai and Z. Hiroi, Successive symmetry breaking in a $J_{\text{eff}} = 3/2$ quartet in the spin-orbit coupled insulator $\text{Ba}_2\text{MgReO}_6$, *J. Phys. Soc. Jpn.* **88**, 064712 (2019).
- [9] D. Hirai, H. Sagayama, S. Gao, H. Ohsumi, G. Chen, T.-h. Arima, and Z. Hiroi, Detection of multipolar orders in the spin-orbit-coupled $5d$ Mott insulator $\text{Ba}_2\text{MgReO}_6$, *Phys. Rev. Res.* **2**, 022063(R) (2020).
- [10] D. Hirai and Z. Hiroi, Possible quadrupole order in tetragonal $\text{Ba}_2\text{CdReO}_6$ and chemical trend in the ground states of $5d^1$ double perovskites, *J. Phys.: Condens. Matter* **33**, 135603 (2021).
- [11] H. Ishikawa, T. Takayama, R. K. Kremer, J. Nuss, R. Dinnebier, K. Kitagawa, K. Ishii, and H. Takagi, Ordering of hidden multipoles in spin-orbit entangled $5d^1$ Ta chlorides, *Phys. Rev. B* **100**, 045142 (2019).
- [12] H. Yun and G.-J. Jang, Dicaesium hexachlorotantalate(IV), Cs_2TaCl_6 , *Acta Crystallographica Section E Structure Reports Online* **63**, i22 (2007).
- [13] M.-T. Suzuki, H. Ikeda, and P. M. Oppeneer, First-principles theory of magnetic multipoles in condensed matter systems, *J. Phys. Soc. Jpn.* **87**, 041008 (2018).
- [14] G. Trimarchi, Z. Wang, and A. Zunger, Polymorphous band structure model of gapping in the antiferromagnetic and paramagnetic phases of the Mott insulators MnO , FeO , CoO , and NiO , *Phys. Rev. B* **97**, 035107 (2018).
- [15] J. Varignon, M. Bibes, and A. Zunger, Mott gapping in $3d\text{ABO}_3$ perovskites without Mott-Hubbard interelectronic repulsion energy U , *Phys. Rev. B* **100**, 035119 (2019).
- [16] A. Mansouri Tehrani and N. A. Spaldin, Untangling the structural, magnetic dipole, and charge multipolar orders in $\text{Ba}_2\text{MgReO}_6$, *Phys. Rev. Mater.* **5**, 104410 (2021).
- [17] G. Kresse and J. Hafner, *Ab initio* molecular dynamics for liquid metals, *Phys. Rev. B* **47**, 558 (1993).
- [18] G. Kresse and J. Furthmüller, Efficient iterative schemes for *ab initio* total-energy calculations using a plane-wave basis set, *Phys. Rev. B* **54**, 11169 (1996).
- [19] G. Kresse and D. Joubert, From ultrasoft pseudopotentials to the projector augmented-wave method, *Phys. Rev. B* **59**, 1758 (1999).
- [20] P. E. Blöchl, Projector augmented-wave method, *Phys. Rev. B* **50**, 17953 (1994).
- [21] J. P. Perdew, K. Burke, and M. Ernzerhof, Generalized Gradient Approximation Made Simple, *Phys. Rev. Lett.* **77**, 3865 (1996).
- [22] S. L. Dudarev, G. A. Botton, S. Y. Savrasov, C. J. Humphreys, and A. P. Sutton, Electron-energy-loss spectra and the structural stability of nickel oxide: An LSDA+ U study, *Phys. Rev. B* **57**, 1505 (1998).
- [23] F. Cricchio, F. Bultmark, O. Grånäs, and L. Nordström, Itinerant Magnetic Multipole Moments of Rank Five as the Hidden Order in URu_2Si_2 , *Phys. Rev. Lett.* **103**, 107202 (2009).
- [24] N. A. Spaldin, M. Fechner, E. Bousquet, A. Balatsky, and L. Nordström, Monopole-based formalism for the diagonal magnetoelectric response, *Phys. Rev. B* **88**, 094429 (2013).
- [25] F. Bultmark, F. Cricchio, O. Grånäs, and L. Nordström, Multipole decomposition of LDA + U energy and its application to actinide compounds, *Phys. Rev. B* **80**, 035121 (2009).
- [26] The Elk Code, <http://elk.sourceforge.net>.
- [27] M. E. Merkel, Multipyles v1.0.0, <https://doi.org/10.5281/zenodo.6907024>.